GOALS-JWST: Gas Dynamics and Excitation in NGC 7469 Revealed by NIRSpec

Marina Bianchin[1,31] , Vivian U[1] , Yiqing Song[2,3] , Thomas S.-Y. Lai (賴劭愉)[4] , Raymond P. Remigio[1] ,
Loreto Barcos-Muñoz[5,6] , Tanio Díaz-Santos[7,8] , Lee Armus[4] , Hanae Inami[9] , Kirsten L. Larson[10] , Aaron S. Evans[5,6] ,
Torsten Böker[11] , Justin A. Kader[1] , Sean T. Linden[12] , Vassilis Charmandaris[7,8,13] , Matthew A. Malkan[14] , Jeff Rich[15] ,
Thomas Bohn[9] , Anne M. Medling[16,17] , Sabrina Stierwalt[18] , Joseph M. Mazzarella[4] , David R. Law[19] ,
George C. Privon[5,6,20] , Susanne Aalto[21] , Philip Appleton[4] , Michael J. I. Brown[22] , Victorine A. Buiten[22] ,
Luke Finnerty[14] , Christopher C. Hayward[23] , Justin Howell[4] , Kazushi Iwasawa[24,25] , Francisca Kemper[24,26,27] ,
Jason Marshall[28] , Jed McKinney[12] , Francisco Müller-Sánchez[29] , Eric J. Murphy[5] , Paul P. van der Werf[22] ,
David B. Sanders[30] , and Jason Surace[4]

[1] 4129 Frederick Reines Hall, Department of Physics and Astronomy, University of California, Irvine, CA 92697, USA; mbianch1@uci.edu
[2] European Southern Observatory, Alonso de Córdova, 3107, Vitacura, Santiago 763-0355, Chile
[3] Joint ALMA Observatory, Alonso de Córdova, 3107, Vitacura, Santiago 763-0355, Chile
[4] IPAC, California Institute of Technology, 1200 E. California Boulevard, Pasadena, CA 91125, USA
[5] National Radio Astronomy Observatory, 520 Edgemont Road, Charlottesville, VA 22903, USA
[6] Department of Astronomy, University of Virginia, 530 McCormick Road, Charlottesville, VA 22903, USA
[7] Institute of Astrophysics, Foundation for Research and Technology-Hellas (FORTH), Heraklion 70013, Greece
[8] School of Sciences, European University Cyprus, Diogenes street, Engomi, 1516 Nicosia, Cyprus
[9] Hiroshima Astrophysical Science Center, Hiroshima University, 1-3-1 Kagamiyama, Higashi-Hiroshima, Hiroshima 739-8526, Japan
[10] AURA for the European Space Agency (ESA), Space Telescope Science Institute, 3700 San Martin Drive, Baltimore, MD 21218, USA
[11] European Space Agency, c/o STScI, 3700 San Martin Drive, Baltimore, MD 21218, USA
[12] Department of Astronomy, University of Massachusetts at Amherst, Amherst, MA 01003, USA
[13] Department of Physics, University of Crete, Heraklion 71003, Greece
[14] Department of Physics & Astronomy, 430 Portola Plaza, University of California, Los Angeles, CA 90095, USA
[15] The Observatories of the Carnegie Institution for Science, 813 Santa Barbara Street, Pasadena, CA 91101, USA
[16] Department of Physics & Astronomy and Ritter Astrophysical Research Center, University of Toledo, Toledo, OH 43606, USA
[17] ARC Centre of Excellence for All Sky Astrophysics in 3 Dimensions (ASTRO 3D), Australia
[18] Physics Department, 1600 Campus Road, Occidental College, Los Angeles, CA 90041, USA
[19] Space Telescope Science Institute, 3700 San Martin Drive, Baltimore, MD 21218, USA
[20] Department of Astronomy, University of Florida, Gainesville, FL 32611, USA
[21] Department of Space, Earth and Environment, Chalmers University of Technology, 412 96 Gothenburg, Sweden
[22] Leiden Observatory, Leiden University, PO Box 9513, 2300 RA Leiden, The Netherlands
[23] Center for Computational Astrophysics, Flatiron Institute, 162 Fifth Avenue, New York, NY 10010, USA
[24] ICREA, Pg. Lluís Companys 23, 08010 Barcelona, Spain
[25] Institut de Ciències del Cosmos (ICCUB), Universitat de Barcelona (IEEC-UB), Martí i Franquès 1, 08028 Barcelona, Spain
[26] Institut de Ciències de l'Espai (ICE, CSIC), Can Magrans, s/n, E-08193 Cerdanyola del Vallès, Barcelona, Spain
[27] Institut d'Estudis Espacials de Catalunya (IEEC), E-08034 Barcelona, Spain
[28] Glendale Community College, 1500 N. Verdugo Road, Glendale, CA 91208, USA
[29] Department of Physics and Materials Science, The University of Memphis, 3720 Alumni Avenue, Memphis, TN 38152, USA
[30] Institute for Astronomy, University of Hawaii, 2680 Woodlawn Drive, Honolulu, HI 96822, USA

Abstract

We present new JWST NIRSpec integral field spectroscopy (IFS) data for the luminous infrared galaxy NGC 7469, a nearby (70.6 Mpc) active galaxy with a Seyfert 1.5 nucleus that drives a highly ionized gas outflow and a prominent nuclear star-forming ring. Using the superb sensitivity and high spatial resolution of the JWST instrument NIRSpec IFS, we investigate the role of the Seyfert nucleus in the excitation and dynamics of the circumnuclear gas. Our analysis focuses on the [Fe II], H_2, and hydrogen recombination lines that trace the radiation/shocked-excited molecular and ionized interstellar medium around the active galactic nucleus (AGN). We investigate gas excitation through $H_2/Br\gamma$ and [Fe II]/$Pa\beta$ emission line ratios and find that photoionization by the AGN dominates within the central 300 pc of the galaxy except in a small region that shows signatures of shock-heated gas; these shock-heated regions are likely associated with a compact radio jet. In addition, the velocity field and velocity dispersion maps reveal complex gas kinematics. Rotation is the dominant feature, but we also identify noncircular motions consistent with gas inflows as traced by the velocity residuals and the spiral pattern in the $Pa\alpha$ velocity dispersion map. The inflow is 2 orders of magnitude higher than the AGN accretion rate. The compact nuclear radio jet has enough power to drive the highly ionized outflow. This scenario suggests that the inflow and

1

outflow are in a self-regulating feeding–feedback process, with a contribution from the radio jet helping to drive the outflow.

Unified Astronomy Thesaurus concepts: Luminous infrared galaxies (946); Galaxy nuclei (609); Active galactic nuclei (16); Seyfert galaxies (1447); Galaxy winds (626); Galaxy kinematics (602); Galaxy dynamics (591)

1. Introduction

Luminous infrared galaxies (LIRGs) are systems with high infrared luminosities ($L_{IR} \geqslant 10^{11} L_\odot$) that, in the nearby Universe, are mostly major mergers (Sanders & Mirabel 1996). These galaxies host extreme environments where both starburst and nuclear activities play a significant role in shaping their evolution (e.g., Hekatelyne et al. 2020). Spatially resolved studies show that gas excitation in LIRGs and their ultra-luminous counterparts (ULIRGs; $L_{IR} \geqslant 10^{12} L_\odot$) is governed by a mixture of processes typical of active galactic nuclei (AGNs; sometimes hidden behind large amounts of dust with an A_V up to ~40; U et al. 2019; Pérez-Torres et al. 2021), star-forming regions, and shocked gas (e.g., Rich et al. 2015; Hekatelyne et al. 2020).

The gas dynamics in (U)LIRGs are often heavily impacted by interactions with other galaxies, the presence of AGNs, and/or starbursts. Evidence for this comes from the detection of outflows on a variety of physical scales and gas phases: cold (Feruglio et al. 2010; Xu et al. 2014; Veilleux et al. 2017; Barcos-Muñoz et al. 2018; Falstad et al. 2018; Lutz et al. 2020; Pereira-Santaella et al. 2020) and hot molecular gas (U et al. 2013, 2019; Medling & Rich 2015; Riffel et al. 2020; Motter et al. 2021), as well as moderately (Rich et al. 2012, 2014, 2015; Arribas et al. 2014; Robleto-Orús et al. 2021; Xu & Wang 2022) and highly ionized gas (Rodríguez-Ardila et al. 2006; Müller-Sánchez et al. 2011; U et al. 2022; Armus et al. 2023) and neutral gas (Rupke & Veilleux 2011; Morganti et al. 2016; Su et al. 2023). Streaming motions, such as gas inflows, toward the nuclear regions of ULIRGs have also been detected in some sources (Hekatelyne et al. 2018; Aalto et al. 2019; Medling et al. 2019; González-Alfonso et al. 2021). These inflows may act in providing the fuel necessary to trigger and feed the AGN.

NGC 7469 hosts a Type I active nucleus (Osterbrock 1977; Peterson et al. 2014) subclassified as Seyfert 1.5 (Landt et al. 2008) located at 70.6 Mpc ($z = 0.01627$) with a (R')SAB(rs)a morphology (de Vaucouleurs et al. 1991). The central kiloparsec region of NGC 7469 shows a bright AGN surrounded by a star-forming ring (e.g., Davies et al. 2004; Díaz-Santos et al. 2007; Song et al. 2021). The ring has inner and outer radii of 330 and 616 pc (see Figure 1), respectively, with a bimodal stellar population as seen from Hubble Space Telescope (HST) imaging (Díaz-Santos et al. 2007) with a star formation rate ~ 22 $M_\odot$ yr^{-1} estimated from its radio continuum (Song et al. 2021), consistent with 10–30 $M_\odot$ yr^{-1} estimated from recombination, [Ne II], and [Ne III] lines (Lai et al. 2022). JWST NIRCam (Rieke et al. 2023) and MIRI (Bouchet et al. 2015) imaging reveal previously undetected embedded stellar clusters with colors that suggest stellar ages of <5 Myr (Bohn et al. 2023). The H_2 polycyclic aromatic hydrocarbon (PAH) flux ratio, which measures the excess H_2 relative to PAHs, is within the range of values from normal photodissociation models, implying that the ring is not currently being affected by AGN feedback (Lai et al. 2022).

NGC 7469 hosts a nuclear outflow traced by highly ionized gas as evidenced in the JWST MIRI-MRS observations (U et al. 2022; Armus et al. 2023) and in the near-infrared via the [Si VI] 1.96 μm emission line (Müller-Sánchez et al. 2011), and

by the moderately ionized gas also traced by MIRI MRS (Zhang & Ho 2023). This outflow has an extent of 400–600 pc and affects mostly the region located between the nucleus and the ring, referred to as the inner interstellar medium (inner-ISM). The outflow has a stratified and decelerating structure as evidenced by highly blueshifted wings on the coronal emission lines (Armus et al. 2023). The warm molecular gas shows enhanced velocity dispersion to the northwest of the central AGN, suggestive of the presence of shocked gas (U et al. 2022). Considering the richness of physical phenomena in its inner kiloparsec region, NGC 7469 is an ideal target to investigate AGN–starburst–ISM interactions.

In this paper, we report the morphology, kinematics, and excitation of the ionized atomic and hot (~1000 K) molecular gas in the central region of NGC 7469 as observed by JWST (Rigby et al. 2023, and references therein) with the NIRSpec instrument in its integral field spectroscopy (IFS) mode. We describe the observations and data reduction in Section 2 and our results in Section 3. We discuss the kinematics and gas excitation in Section 4 and present our conclusions in Section 5.

2. Data

2.1. JWST NIRSpec Observations

NGC 7469 was observed with NIRSpec IFS (Böker et al. 2022; Jakobsen et al. 2022) on 2022 July 19 as part of the JWST Director Discretionary Time Early Release Science (DD-ERS) program (PID: 1328, PIs: Lee Armus and Aaron Evans). We employed NIRSpec in the high-resolution mode ($R \approx 2700$, corresponding to a velocity resolution of ≈ 110 km s^{-1}) in three grating/filter combinations—G140H/F100LP, G235H/F170LP, and G395H/F290LP—covering the wavelength range of 0.97–5.27 μm with a nominal field of view (FOV) of $3'' \times 3''$ (see Figure 1). In order to cover the star-forming ring fully (~4'' across), we used the large cycling four-point dither pattern, which provides a FOV of $4\rlap{.}''2 \times 4\rlap{.}''8$, corresponding to 1.4×1.6 kpc^2 at the distance of NGC 7469 (Figure 1). For extended targets, MSA leakage correction (leakcal) exposures are necessary to account for the leakage from the permanently open microshutters. While observing NGC 7469, we used the same dither pattern for the leakcals as we did for the science observations. The science exposure time in each grating/filter combination is 817 s and the total observing time, including the leakcals and overheads, is 10.5 ks.

2.2. Data Reduction

We reduce the level-1 data downloaded from MAST using the JWST pipeline v1.8.3 (Bushouse et al. 2022) in batch mode. The reference files follow the context version `jwst_12027.pmap`. The first reduction step is `Detector1`, which generates rate files with a detector-level correction applied to them. Both science and leakage calibration files are processed at the `Detector1` step. The second reduction step for spectroscopic data is `Spec2`, which applies distortion, wavelength, and flux calibrations, and other 2D corrections to the science data, including leakage subtraction.
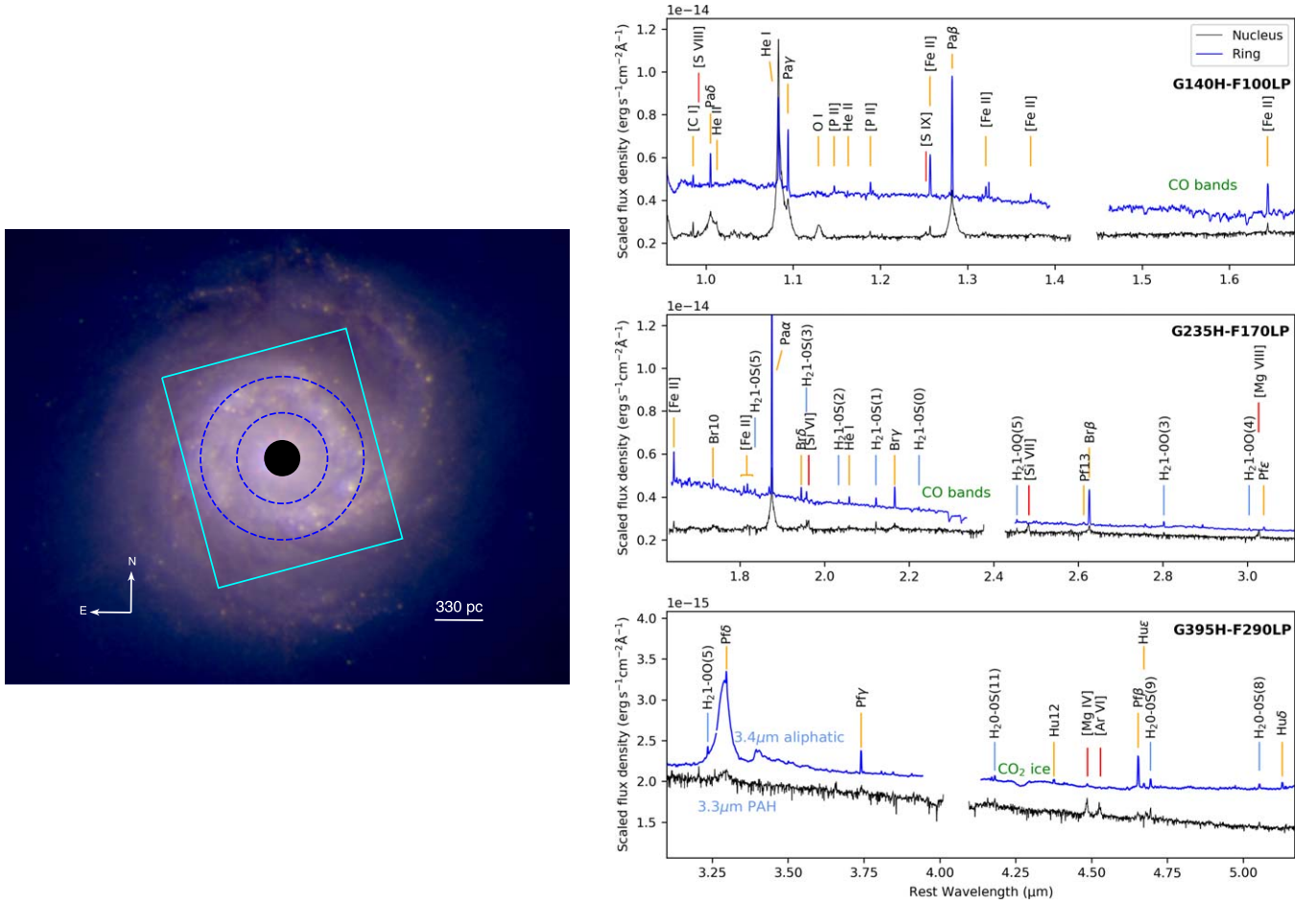
Figure 1. Left: HST (F110W) and JWST (F150W and F200W) color composite image of NGC 7469 (Bohn et al. 2023). North is up and east to the left, as indicated by the compass in the bottom left. Bright stellar clusters are detected throughout the starburst ring. The cyan rectangle indicates the combined field of view (FOV) of our dithered NIRSpec observations ($4.''2 \times 4.''8$). $1''$ corresponds to 330 pc at the distance of the galaxy. The right panels show extracted NIRSpec spectra from the nucleus with a radius of $0.''4$ (black) and the star-forming ring with inner and outer radius of $1''$ and $1.''8$ (blue). These extractions correspond to the black-filled circle and the dashed blue annulus in the galaxy image, respectively. The red, orange, and light blue lines indicate the location of the high ionization (coronal), the ionized, and molecular emission lines, respectively. The spectra were arbitrarily scaled for visualization purposes to differentiate between the nuclear and the star-forming ring spectra. The first shows the broad lines, typical of Type 1 nuclei, in the permitted emission lines as the hydrogen and helium recombination lines, high ionization coronal lines indicated by the red markers, and other emission lines such as [Fe II] and H_2. The latter is dominated by narrow lines, a prominent PAH feature at 3.3 μm close to an aliphatic feature at 3.4 μm, CO stellar absorption features, and CO_2 absorption.

The outlier rejection algorithm is not efficient in the current version of the pipeline. Most of the outliers have fluxes higher than the typical flux of the brighter emission lines or show negative flux values. We optimized the outlier rejection by flagging spectral pixels that showed clear contamination in the calibrated science frames (Hutchison et al. 2023). These corrected frames are then fed to the last reduction step Spec3 that builds the data cubes by combining individual exposures taken at each dither position. We obtain three data cubes corresponding to each grating and filter combination: G140H/100LP, G235H/170LP, and G395H/290LP.

In order to correct the pipeline-processed cubes for astrometry we adopt the peak of the continuum in each cube as the position of the nucleus. We then modify the NIRSpec IFS data cube headers to align with the continuum peak of the CH1-short MIRI-MRS cube. Our final data cubes have a spatial resolution of $0.''14$ at 1.12 μm, as obtained from the FWHM of the O I 1.12 μm emission line image, allowing us to resolve structures down to $\sim$50 pc at this wavelength. The spatial resolution is poorer at longer wavelengths, as demonstrated by

Lai et al. (2023), who measure a spatial resolution of $0.''19$ for dust features at 3.3 μm.

3. Analysis and Results

The right panels of Figure 1 show two spectra extracted from the nucleus ($0.''4$ radius, in black) and from the star-forming ring ($1''$–$1.''8$ radii, in blue) in NGC 7469. In the nuclear spectrum, we detect prominent emission from hydrogen recombination lines, particularly broad components in the Paschen series, and permitted lines such as O I and He II. This broad component may be associated with the broad-line region of AGNs and is typical of Type 1 sources. The nuclear spectrum also features coronal lines such as in [Si VII] and [Mg VIII] with blueshifted profiles, similar to observations of higher ionization coronal lines from Armus et al. (2023), indicative of gas outflows. Narrow lines such as [Fe II], H_2, and the PAH band at 3.3 μm are only weakly detected. The strong continuum radiation from the AGN might be the cause for the reduced equivalent width of these lines at the nucleus. On the other hand, PAH features and CO absorption bands are featured

Table 1
Emission Line Fluxes of the Nucleus and Star-forming Ring in the G140H Grating

Line	λ_{rest}	IP	Nucleus	Ring
[C I]	0.985	⋯	4.56 ± 0.75	2.35 ± 0.82
Paδ	1.005	⋯	77.18 ± 8.31	14.81 ± 1.51
He II	1.012	24.6	22.9 ± 7.4	⋯
He I	1.083	⋯	451.52 ± 2.03	57.86 ± 3.54
Paγ	1.094	⋯	122.67 ± 2.02	31.64 ± 2.7
O I	1.129	⋯	36.86 ± 1.57	⋯
[P II]	1.147	10.5	⋯	2.88 ± 1.24
[P II]	1.188	10.5	2.44 ± 0.07	5.26 ± 1.24
[S IX]	1.252	328.8	4.46 ± 0.39	⋯
[Fe II]	1.257	7.9	6.62 ± 0.24	27.15 ± 1.19
Paβ	1.281	⋯	153.6 ± 1.84	75.52 ± 1.1
[Fe II]	1.321	7.9	3.24 ± 0.36	8.52 ± 2.25
[Fe II]	1.372	7.9	⋯	4.6 ± 2.25
[Fe II]	1.644	7.9	6.76 ± 1.37	25.56 ± 0.25

Note. Rest wavelengths (λ_{rest}) are in units of μm, the ionization potentials (IPs) are in units of eV, and all fluxes are in units of 10^{-15} erg s^{-1} cm^{-2}.

Table 2
Emission Line Flux Densities of the Nucleus and Star-forming Ring in the G235H Grating

Line	λ_{rest}	IP	Nucleus	Ring
Br10	1.7636	⋯	⋯	6.94 ± 1.39
$H_2$1-0S(5)	1.835	⋯	⋯	2.97 ± 1.61
Paα	1.875	⋯	224.31 ± 0.23	246.57 ± 1.28
Brδ	1.945	⋯	⋯	9.84 ± 1.28
$H_2$1-0S(3)	1.957	⋯	7.65 ± 0.03	7.48 ± 1.49
[Si VI]	1.963	166.8	14.35 ± 0.06	⋯
$H_2$1-0S(2)	2.033	⋯	⋯	3.69 ± 1.51
He I	2.058	⋯	1.9 ± 0.09	6.59 ± 0.97
$H_2$1-0S(1)	2.122	⋯	7.39 ± 0.41	11.23 ± 1.4
Brγ	2.166	⋯	30.44 ± 2.67	24.51 ± 1.21
$H_2$1-0S(0)	2.223	⋯	⋯	6.77 ± 1.4
$H_2$1-0Q(5)	2.454	⋯	2.99 ± 0.61	⋯
[Si VII]	2.483	205.3	17.93 ± 0.96	⋯
Brβ	2.625	⋯	36.99 ± 6.84	44.29 ± 1.85
$H_2$1-0O(3)	2.802	⋯	⋯	7.75 ± 2.15
[Mg VIII]	3.027	225.2	17.07 ± 0.28	⋯
Pfζ	3.039	⋯	⋯	3.68 ± 1.25

Note. Rest wavelengths (λ_{rest}) are in units of μm, the IPs are in units of eV, and all fluxes are in units of 10^{-15} erg s^{-1} cm^{-2}.

Table 3
Emission Line Flux Densities of the Nucleus and Star-forming Ring in the G395H Grating

Line	λ_{rest}	IP	Nucleus	Ring
$H_2$1-0O(5)	3.235	⋯	⋯	5.3 ± 0.59
Pfε	3.297	⋯	⋯	5.17 ± 1.68
Pfδ	3.740	⋯	12.36 ± 2.98	10.56 ± 0.2
$H_2$0-0S(11)	4.181	⋯	2.07 ± 0.15	2.81 ± 0.25
Hu12	4.376	⋯	⋯	3.1 ± 0.38
[Mg IV]	4.486	80.1	13.51 ± 0.59	0.79 ± 0.22
[Ar VI]	4.529	74.8	8.97 ± 0.57	⋯
Pfγ	4.653	⋯	1.34 ± 0.32	18.56 ± 0.25
Huε	4.672	⋯	⋯	2.59 ± 0.25
$H_2$0-0S(9)	4.694	⋯	3.29 ± 0.27	5.38 ± 0.25
$H_2$0-0S(8)	5.053	⋯	1.31 ± 0.27	2.49 ± 0.1
Huδ	5.128	⋯	⋯	3.27 ± 0.1

Note. Rest wavelengths (λ_{rest}) are in units of μm, the IPs are in units of eV, and all fluxes are in units of 10^{-15} erg s^{-1} cm^{-2}.

Due to the undersampling of the point-spread function (PSF) in the NIRSpec IFS mode, the per-spaxel spectra in the nuclear region exhibit a wiggly pattern that is different from the fringes characteristic of 1D spectra extracted from MRS data. To mitigate this effect, we use a spectrum averaged over an aperture with a radius of 0″.2 as representative of the nuclear region. The chosen aperture size is motivated by the size of the PSF.

In order to obtain emission line moment maps, we use the Python package IFSCUBE (Ruschel-Dutra & Dall'Agnol De Oliveira 2020; Ruschel-Dutra et al. 2021) to fit the emission lines of interest with Gaussian functions and the underlying continuum with a polynomial function in each spaxel of the data cube. We fit a broad component ($\sigma \approx 890$ km s^{-1} at systemic velocity, corresponding to FWHM ≈ 2095 km s^{-1} in agreement with Lu et al. 2021) typical of Type 1 AGNs, and a narrow component to the hydrogen recombination lines. In the case of the Paα line, an extra component was necessary to reproduce the broad ($\sigma \approx 800$ km s^{-1}) emission line observed beyond the PSF extension, likely associated with a gas outflow. A single narrow component is enough to reproduce the emission line profiles of the forbidden and molecular hydrogen lines. A third-degree polynomial reproduced the underlying continuum of spectra obtained with the G140H and G235H gratings. The fitting for spectra from each grating is performed independently, but within each grating spectrum, we tie the systemic velocity and velocity dispersion of the lines that trace the same gas phase.

3.1. Flux and Line Ratios

The resulting moment maps from our spectral fitting procedure for three emission lines representative of the atomic ionized—[Fe II] 1.257 μm and Paα—and the molecular gas—H_2 2.12 μm—phases are shown in Figure 2. Both [Fe II] and Paα have low ionization potentials (IPs), with IP = 7.9 eV and 13.6 eV, respectively, and the integrated flux maps show that they trace the star-forming ring and the point source at the nucleus. The ring has knots of star formation (SF) to the north, west, and south, but is fainter and more flocculent to the east of the nucleus. The 0″.2 resolution of NIRSpec at 1.9 μm reveals a tail southeast of the nucleus in the inner-ISM region that, in projection, connects the ring to the AGN as seen in the Paα
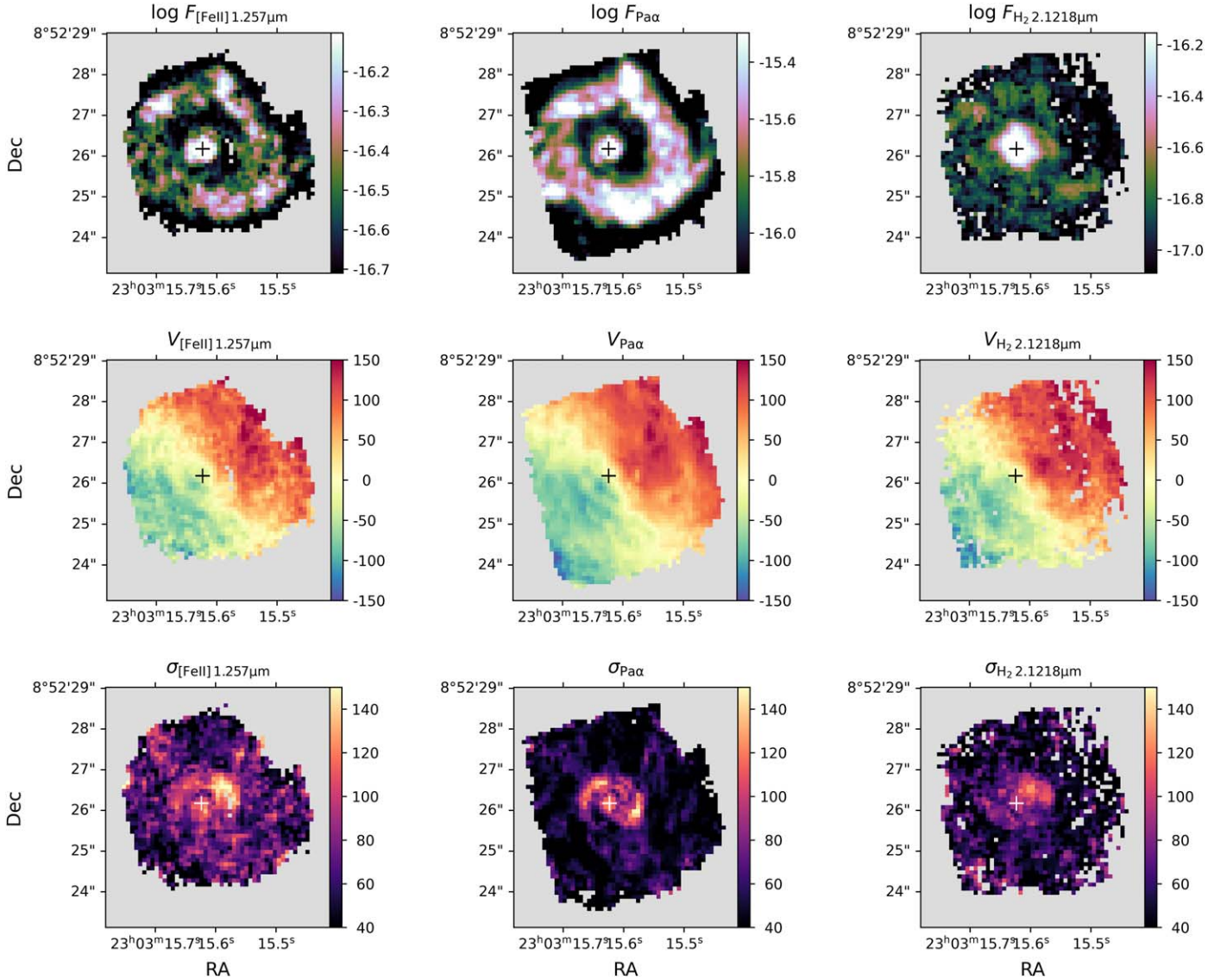
prominently in the ring spectrum, while coronal lines and the broad component of the H recombination lines disappear. We also see other ionized gas species such as [P II] and [Fe II], as well as various H_2 transitions in the ring. Tables 1, 2, and 3 present the emission line integrated fluxes for each grating in both the nuclear and ring extractions. The fluxes are obtained by fitting one, or two in the case of recombination and coronal lines, Gaussian functions to each line, and a polynomial to the continuum. Only the lines with at least a 3σ detection in each extraction are included. The fluxes of the 3.3 μm PAH and aliphatic feature are part of our companion paper (Lai et al. 2023), which discusses the dust grain distribution in NGC 7469 in detail.

For the present paper, we focus our analysis on a subset of the emission lines observed (i.e., [Fe II], H_2, and the H I lines) to highlight the conditions of the multiphase ISM.

Figure 2. Flux (top row, in units of erg s^{-1} cm^{-2}, in logarithmic scale), velocity (middle row, in units of km s^{-1}), and velocity dispersion (bottom row, in units of km s^{-1}) of three emission lines: [Fe II] 1.257 μm, Paα, and H$_2$ 2.1218 μm. The cross indicates the position of the nucleus across all the panels. North is up and east is to left. A connection between the ring and the nucleus, to the southeast of the latter, is observed in the Paα flux map. The gas motions are dominated by rotation, but noncircular motions also contribute to the gas dynamics, as evidenced by the excesses of blueshift and redshifts to the southeast and northwest of the nucleus, respectively, and regions with enhanced velocity dispersion close to the nucleus, but with different morphologies for the three emission lines. The locations of the enhanced velocity dispersion are signatures of gas disturbed by the outflow, for [Fe II] and H$_2$, or gas heated by friction in an inflow, for the Paα. See Section 4.2 for discussion.

flux map (see Figure 2). The inner-ISM region has a surface brightness around an order of magnitude lower than the ring and the nucleus, indicating that the excitation/heating of the gas might be different in this region. The H$_2$ flux is more concentrated at the center where the peak of the emission is also observed. It does not show a ring-like pattern; instead, it displays a more extended and diffuse morphology, resembling a spiral arm to the southwest as previously noticed in the warm molecular phase with MIRI (U et al. 2022) and cool CO gas (Davies et al. 2004). Both H$_2$ 2.12 μm and H$_2$ 1.95 μm fluxes have this distribution.

In order to investigate the origin of the gas emitted in the central region of NGC 7469, we create emission line ratio maps of H$_2$/Brγ and [Fe II] 1.257 μm/Paβ (Figure 3, panels (a) and (b)), which are insensitive to extinction. The ring shows low line ratio values ~0.5 for both H$_2$/Brγ and [Fe II] 1.257 μm/Paβ.

The H$_2$/Brγ has the highest values (~3.5) at the nucleus and in the western inner-ISM region. [Fe II]/Paβ is also the highest in the latter. The gray regions correspond to spaxels where at least one of the two lines in the ratio has a signal-to-noise ratio (S/N) lower than 2. In the inner-ISM region, the low S/N spaxels are attributed to Paβ and Brγ nondetections.

The excitation diagram (Figure 3 (c)) shows data points based on the emission line ratios presented in panels (a) and (b). To distinguish among the different mechanisms that regulate these line ratios, we use the thresholds derived by Riffel et al. (2013), and color code the spaxels depending on their location on the excitation diagram (panel (d)). These boundaries are derived from analyzing single-slit spectra of galaxies previously classified as starbursts, AGN hosts, or shock-dominated sources such as LINERS. The division between AGN low excitation and AGN high excitation is
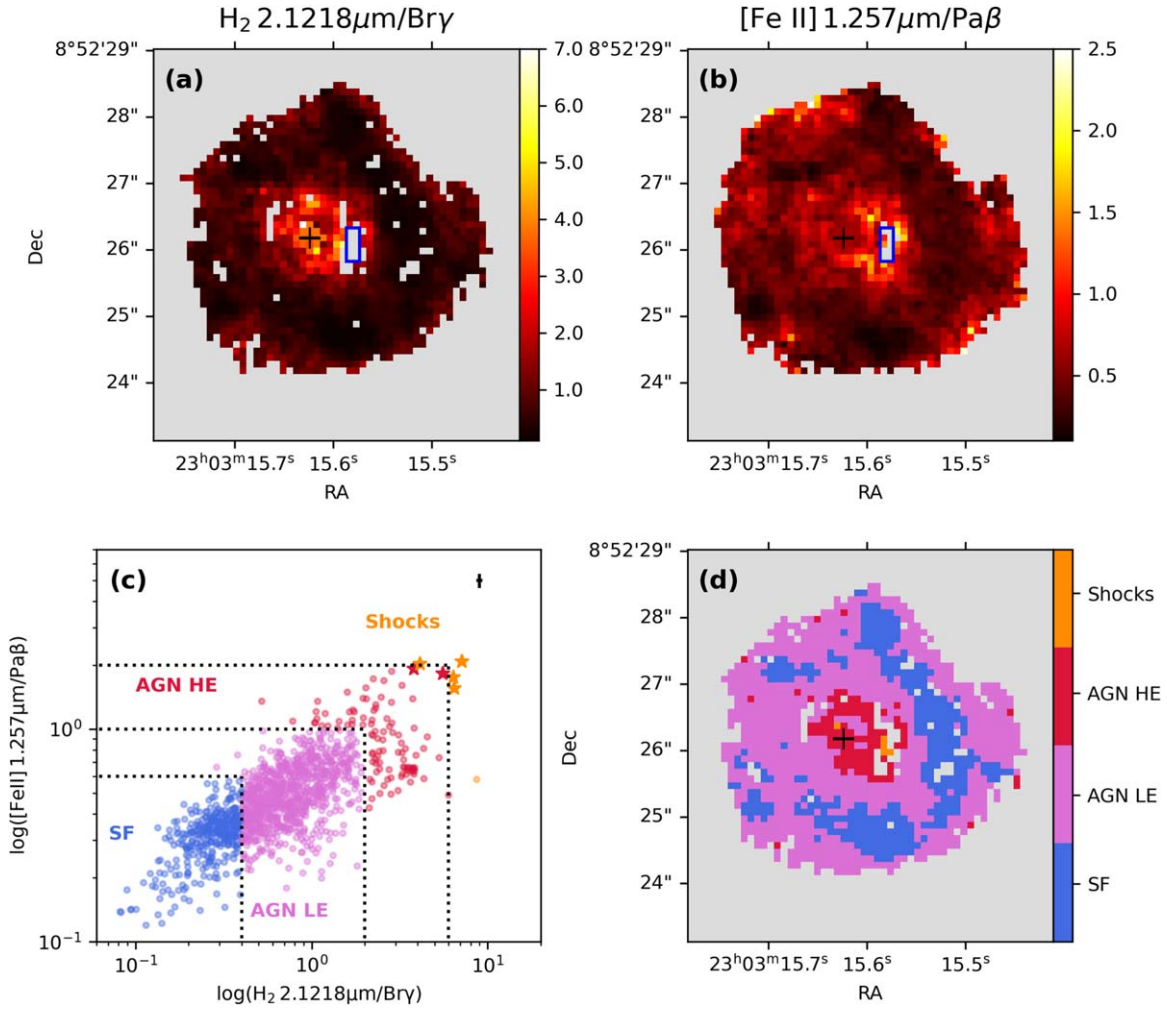
Figure 3. Line ratio diagnostics in the near-infrared: H₂ 2.1218 μm/Brγ (a) and [Fe II] 1.257 μm/Paβ (b). Given that the Paβ and Brγ lines in the inner-ISM region are only marginally detected (S/N < 2), lower limits of the H₂/Brγ and [Fe II]/Paβ ratios are estimated using the values inside the blue boxes and presented as the star symbols in the near-infrared excitation diagnostic diagram (c). The bottom panels show the near-infrared excitation diagram ((c): adapted from Riffel et al. 2013) and the corresponding spatial location of spaxels dominated by different excitation (d). The spaxels are color coded by their location on the excitation diagram: SF, AGN low excitation (LE), AGN high excitation (HE), and shocks. The line ratios encompass the complexity of the gas excitation in the inner kiloparsec of NGC 7469, where evidence of SF and the AGN radiation field and HE due to shocks are present. The typical uncertainties in both line ratios are indicated in the top right corner of panel (c).

motivated by allowing for a finer sampling of the AGN influence on spatial scales. We use [Fe II] 1.257 μm/Paβ = 1 and H₂ 2.12μm/Brγ = 2 as adopted by Riffel et al. (2021b), which are arbitrary.

Since the recombination lines have low fluxes in the inner-ISM region and the H₂ is detected in the same region, we expect high line ratios in the western part of the nucleus. The blue box overlaid in the line ratio maps indicates the region where we extracted average spectra for the G140H and G235H gratings. From these spectra, we obtain upper limits for the Brγ and Paβ emission lines. The ratios are then obtained using the flux per spaxel from our H₂ and [Fe II] maps and are plotted on the excitation diagram as stars, indicating they are lower limits on the H₂ 2.12 μm/Brγ ratio.

Applying the color coding from the excitation diagram to the excitation map (Figure 3, panel (d)), we find that the spaxels with the largest flux ratios are consistent with photoionization by the AGN. A small number of spaxels may be shock excited. The inner-ISM region has line ratios consistent excitation by the AGN radiation field and by shocks. With the exception of

the star-forming ring itself, the bulk of the ISM probed by the NIRSpec IFS is photoionized by the AGN.

3.2. Velocity and Velocity Dispersion

In the [Fe II] 1.257 μm, Paα, and H₂ 2.1218 μm velocity fields (middle row of Figure 2), rotation is the dominant feature, with amplitudes of up to 150 km s⁻¹. The rotating disk of hot H₂ we measure was first detected with adaptive optics spectroscopy on the Keck telescope (Hicks & Malkan 2008). That study found similar rotation velocities to what we see: 100 km s⁻¹ or more out to a radius of about 0.″8, almost reaching the starburst ring. Small-scale kinematic features are also observed as excess blueshifts to the southeast and redshifts to the northwest of the nucleus. The velocity field for Paβ (not presented here) shows very similar kinematics and gas distribution as those of Paα, although with a lower S/N.

The velocity dispersion maps show some interesting features previously seen at lower resolution in MIRI-MRS data (U et al. 2022). The ring and outer parts have low dispersion values (∼60–80 km s⁻¹) indicating that they are dominated by rotation.
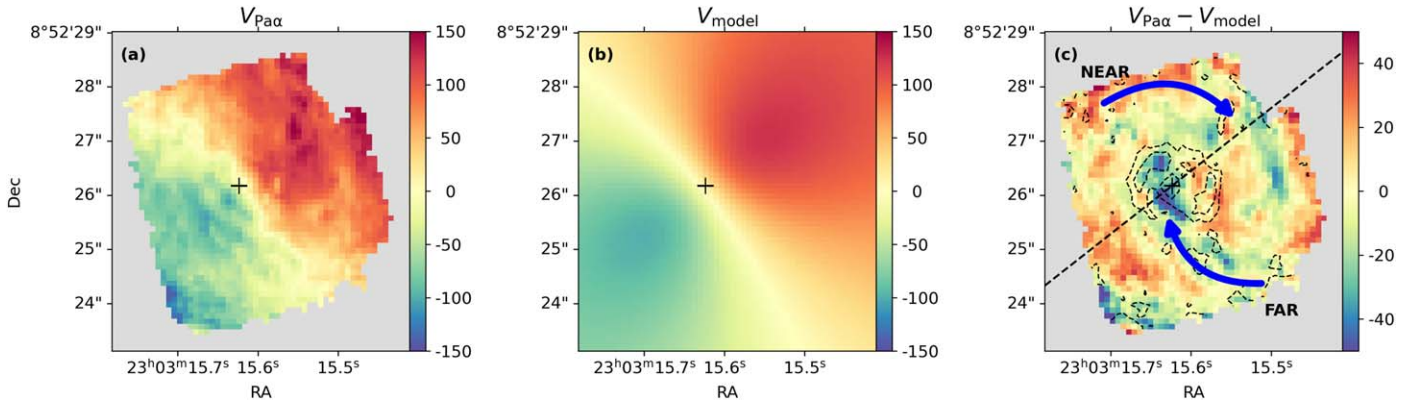
Figure 4. Left to right: Observed Paα velocity field, modeled velocity field with rotation described by a thin disk model, and the residual map from the difference between the observed and modeled velocity fields. The dashed line indicates the direction of the galaxy's kinematic major axis. The near and far sides of the disk are labeled, and the arrows indicate the location of gas that does not follow the galactic rotation and may be inflowing to the nucleus. The contours show the regions of increased velocity dispersion in Paα.

In the inner-ISM region, we see differences between the gas species. The [Fe II] velocity dispersion map shows an arc-shaped structure, with the highest values ($\sigma \approx 140$ km s^{-1}) to the west of the nucleus. For Paα we also see arc-shaped structures peaking in two different regions, to the northeast and southwest of the nucleus, with a dual-spiral pattern. Each of the spirals is located $\sim 0\farcs6$ (≈ 200 pc) away from the nucleus. We investigate the nature of this feature in Section 4.2. The H$_2$ velocity dispersion map displays higher values ($\sigma \approx 120$ km s^{-1}) extending $0\farcs9$ northwest of the nucleus. This feature is also seen in the H$_2$ 1.95 μm velocity dispersion map (not presented here). The fan-shaped feature is consistent with the regions of enhanced H$_2$ dispersion seen with MIRI MRS (U et al. 2022) but at a higher spatial resolution.

One way of investigating the nonrotational motions is by fitting the velocity fields with a rotating disk model that assumes the gas particles have circular orbits. We adopt the model described by the following equation (Bertola et al. 1991):

$$V = V_{\rm sys}$$
$$+ \frac{AR\cos(\psi - \psi_0)\sin\theta\cos^p\theta}{\{R^2[\sin^2(\psi - \psi_0) + \cos^2(\theta)\cos^2(\psi - \psi_0)] + C_0\cos^2\theta\}^{p/2}},$$

where $V_{\rm sys}$ is the systemic velocity of the galaxy, R is the distance of each pixel to the center of rotation, A is the velocity amplitude, ψ is the position angle of each spaxel, ψ_0 is the PA of the line of the nodes, i.e., the kinematical major axis, and θ is the inclination of the disk. The parameter p is the slope of the rotation curve, varying from one for an asymptotically flat rotation curve to 1.5 for a system with finite mass. C_0 is the concentration parameter, the radius where the velocity reaches 70% of the velocity amplitude.

We fit this model to the Paα velocity field as this emission line has the most interesting structure. The fitting is performed using the nonlinear least-square minimization routine `mpfit2dfun` (Markwardt 2009). The combination of parameters that best describe the velocity field are $A = 476.9 \pm 6.09$ km s^{-1}, $V_{\rm sys} = 13.29 \pm 0.41$ km s^{-1}, $C_0 = 0\farcs53 \pm 0\farcs01$, $\psi_0 = 128\fdg81 \pm 0.38$, and $\theta = 15\fdg97 \pm 0.28$. The position of the center of rotation is adopted as the position of the nucleus and $p = 1.5$; both are fixed during the fitting. Previous studies have estimated similar values for Ψ_0 (Davies et al. 2004; Hicks & Malkan 2008; U et al. 2022) and θ (Hicks & Malkan 2008).

Figure 4 shows the modeled velocity field in panel (b), and the residual velocity map, with the position angle of the galaxy's major kinematic axis marked by the black dashed line, in panel (c). "NEAR" and "FAR" indicate the orientation of the star-forming ring proposed by U et al. (2022) and seen in the optical large-scale image of the galaxy. We observe most of the velocity residuals as blueshifts on the far side of the galaxy. Such a configuration may represent streaming motions toward the center.

4. Discussion

4.1. Gas Excitation

Emission line diagnostic diagrams are powerful tools to investigate the origin of emission lines in galaxies. In the near-infrared, empirical diagrams involving bright lines in the J and K bands have been analyzed in single-aperture (Larkin et al. 1998; Reunanen et al. 2002; Rodríguez-Ardila et al. 2004, 2005; Riffel et al. 2013) and spatially resolved studies (Colina et al. 2015; U et al. 2019; Riffel et al. 2021a). The H$_2$ can be excited by soft UV photon absorption (nonthermal) or by collisional excitation (thermal). The thermal processes include shocks (Hollenbach & McKee 1989; Riffel et al. 2015), and X-ray heating by the AGN radiation field. The [Fe II] is produced in the partially ionized region that, in AGN hosts, is a byproduct of X-rays or shocks due to a radio jet or gas outflows (Forbes & Ward 1993; Simpson et al. 1996). Another source of excitation of the [Fe II] is due to shocks caused by supernova remnants, especially in star-forming regions (Rosenberg et al. 2012). Previous studies show that there is a correlation between H$_2$/Brγ and [Fe II]1.257 μm/Paβ, suggesting that both [Fe II] and H$_2$ may have a common excitation mechanism (Larkin et al. 1998; Riffel et al. 2013, 2021a). A positive trend is observed in Figure 3(c), suggesting that in NGC 7469 [Fe II] and H$_2$ are excited by a common mechanism.

The excitation map (Figure 3(d)) shows the spatial distribution of the different line ratios. At the location of the ring, the excitation conditions show a discontinuity to the east, where AGN-like excitation dominates. A morphological discontinuity in the ring, at the same location, has previously been claimed as the result of an outflow-excavated ring (García-Bernete et al. 2022). However, we do not see clear velocity signatures consistent with outflowing gas in the spectral transitions we analyze here.

The highest line ratios (color coded as red and orange) are distributed mostly in the western part of the inner-ISM. These line ratios are indicative of shock-excited gas at the same location as in the MIRI-MRS observations of NGC 7469 (U et al. 2022). The authors linked the shock-excited H_2 with a fan-shaped H_2 S(5) velocity dispersion map. The lower right panel in Figure 2 shows a more clumpy structure than in H_2 S(5). Shock models suggest that regions with fast motions would be expected in a clumpy turbulent medium (Appleton et al. 2023). Thus, the high-velocity dispersion and the shock-like line ratios are indicators of the same shocked gas structure at the western part of the inner-ISM.

NGC 7469 has a compact radio jet–core structure that extends east–west for ∼100 pc, which has been resolved with very long baseline interferometric observations (Lonsdale et al. 2003; Alberdi et al. 2006) and high-resolution Very Large Array observations (Orienti & Prieto 2010; Song et al. 2022) at multiple frequencies. [Fe II] is likely excited by shocks due to interaction of the jet with the ISM in the regions color coded in orange in Figure 3. However, excitation by the AGN radiation field cannot be ruled out, as the jet is compact and line ratios consistent with excitation by the AGN are observed over all the FOV. The ring does show line ratios typical of star-forming galaxies, where nonthermal processes (UV fluorescence) might be the mechanism responsible for the H_2 excitation. The [Fe II] emission observed in the star-forming ring is likely due to shocks caused by supernovae where the dust grains trapping the Fe are destroyed by the supernova remnant shocks (Rosenberg et al. 2012).

4.2. Gas Dynamics: Inflows and the Feedback Driving Mechanism

In Figure 2, the velocity dispersion of Paα shows a dual-spiral pattern, which also appears to exhibit enhanced $H_2/Br\gamma$ and [Fe II]/Paβ ratios. With optical observations of the AGN host Mrk 590, Raimundo et al. (2019) observe a nuclear dual-spiral pattern in the velocity dispersion and flux maps of optical ionized gas emission lines. The authors interpret this pattern as due to a gas inflow to the nucleus of the galaxy. Another example of a nuclear dual spiral is interpreted as a gas inflow in NGC 6951 (Storchi-Bergmann et al. 2007). In the case of NGC 7469, the hypothesis of an inner dual spiral was proposed by Davies et al. (2004) to explain the morphology of the CO(2–1) flux distribution. However, the authors did not find kinematic signatures that could be associated with a gas inflow. In magnetohydrodynamical simulations, stellar feedback from a star-forming ring provides the fuel for gas inflows that starts and sustains the AGN duty cycle (Clavijo-Bohórquez et al. 2024), which is probably the case in NGC 7469. We investigate possible deviations from pure circular rotation by inspecting the velocity residuals in Figure 4 (c). The resolving power of the NIRSpec integral field unit (IFU) at the wavelength of the Paα line is $R \approx 2200$ (Jakobsen et al. 2022), which corresponds to a velocity resolution of ≈ 130 km s^{-1}. The residuals are more prominent closer to the nuclear spiral, reaching 64 km s^{-1} in blueshifts and patchy and with lower amplitudes in the outer regions of the field. The localized nature of the highest residuals in arm-shaped morphology leads us to interpret them as a signature of gas inflow. Similar approaches have been adopted in the literature previously (e.g., Schnorr-Müller et al. 2016, 2017; Riffel et al. 2023a).

If we indeed are observing inspiraling gas, we follow Storchi-Bergmann et al. (2007) and compute the mass inflow rate via:

$$\dot{M}_{in} = N_e V_{in} A m_p f n_{arms}, \tag{1}$$

where N_e is the electron density, V_{in} is the velocity of the inflowing gas, A is the area of the cross section of the spiral arm, m_p is the proton mass, f is the filling factor, and n_{arms} is the number of arms (in our case $n_{arms} = 2$). We estimate the filling factor considering that:

$$L_{Pa\alpha} = f j_{Pa\alpha}(T) v, \tag{2}$$

where $L_{Pa\alpha}$ and $j_{Pa\alpha}(T)$ are the luminosity and emission coefficients of the Paα line (Osterbrock & Ferland 2006), respectively, and v is the volume of the emitting region. Assuming a typical density of 500 cm^{-3} and a temperature of 10,000 K, we determine $j_{Pa\alpha} = 8.29 \times 10^{-22}$ erg cm^{-3} s^{-1}. The Paα luminosity is estimated from the flux map in Figure 2 as 2.4×10^{41} erg s^{-1}. Since most of the Paα emission is associated with the star-forming ring, we assume that half of the line flux comes from the gas inflowing to center as $L_{Pa\alpha} = 1.2 \times 10^{41}$ erg s^{-1}. Assuming that the inflowing gas is distributed in a dual-spiral structure where one of the arms can be represented by a cylinder of height $h = 1.''5$ and radius $r = 0.''3$, the filling factor is $f = 0.14$. This value is higher than previously estimated in the nearby Seyfert galaxy NGC 6951, $f = 0.004$ (Storchi-Bergmann et al. 2007). The mass inflow calculation adopts both filling factor values. The velocity is corrected by the inclination of the galaxy ($V_{in} = \frac{V_{res}}{\sin i}$). From the rotation model residuals (Figure 4, panel (c)) $V_{res} \approx 40$ km s^{-1}. We consider two possible inclinations for NGC 7469: $i = 16°$ derived from the rotation model and $i = 51°$ the inclination of the ring (U et al. 2022). The deprojected inflow velocity is $V_{in} = 51$–145 km s^{-1}.

Considering all the assumptions mentioned above, the mass inflow rate is $\dot{M}_{in} = 0.2$–17 $M_\odot$ yr^{-1}. This value is comparable to the mass outflow rate estimated from the coronal emission lines (1–5 $M_\odot$ yr^{-1}; Müller-Sánchez et al. 2011; Armus et al. 2023). The mass inflow rate is at least 1 order of magnitude larger than the accretion rate needed to power the AGN ($\sim 4.1 \times 10^{-2}$ $M_\odot$ yr^{-1}; Armus et al. 2023). Part of the gas mass moving toward the center might not feed the supermassive black hole and could, in fact, be ejected as part of the outflow.

The fitting of the brightest hydrogen recombination line (Paα) observed in NGC 7469 NIRSpec IFS data reveals the presence of a compact ($R = 0.''6 \equiv 205$ pc), high dispersion ($\sigma = 800$ km s^{-1}) at systemic velocity ($V = 11$ km s^{-1}). We interpret this component as an outflow, as is expected from the presence of gas outflows in highly (Müller-Sánchez et al. 2011; Armus et al. 2023) and moderately (Xu & Wang 2022) ionized gas in this galaxy. In order to investigate the impact of this outflow in the galaxy, we proceed to calculate the mass outflow rates following two different methods. The first follows Equation (4) in Bianchin et al. (2022; see also Harrison et al. 2014; Fiore et al. 2017; Kakkad et al. 2020; Riffel et al. 2023b). The ionized outflow gas mass ($M_{out} \approx 10^6$ $M_\odot$) is obtained by adapting Equation (5) from Storchi-Bergmann et al. (2009) where $F_{Pa\alpha}/F_{Br\gamma} = 12.19$, assuming the case B recombination, a temperature of 10,000 K, and an electron density of 500 cm^{-3}.

The resulting mass outflow rate is $\dot{M}_{out} = 0.18\ M_\odot\ \mathrm{yr}^{-1}$. The second method follows Müller-Sánchez et al. (2011) and Armus et al. (2023), where we use the same electron density as in the first method and a filling factor $f = 0.001$. Instead of the biconical geometry adopted by Armus et al. (2023), we adopt a spherical geometry due to the lack of evidence of a biconical structure in the outflow. The resulting mass outflow following this method is $\dot{M}_{out} = 0.14\ M_\odot\ \mathrm{yr}^{-1}$, in good agreement with the previous method. This mass outflow is consistent with the values derived from the analysis of the outflows traced by the Paβ emission line in local Seyferts (Bianchin et al. 2022).

The mechanical impact of the outflow in the ISM can be accessed via its kinetic power determined by $\dot{E}_{out} = \dot{M}_{out}(V_{max}^2 + 3\sigma^2)/2$. The σ^2 term is particularly important for this case, as most of the energy is associated with turbulent motion. Adopting the velocity, velocity dispersion, and mass outflow rates determined previously, $\dot{E}_{out} = 5.9\text{–}7.2 \times 10^{36}\ \mathrm{erg\ s}^{-1}$. In order to determine if the small-scale radio jet–core structure is capable of driving a highly ionized gas outflow, we follow Morganti et al. (2015) and Venturi et al. (2021) and adopted the scaling relations between the 1.4 GHz radio luminosity and jet power presented in Bîrzan et al. (2008) and Cavagnolo et al. (2010). The jet component has flux density of 9.4 mJy at 8 GHz (Alberdi et al. 2006), and 1.3 mJy at 33 GHz (Song et al. 2022), which yield a 8–33 GHz spectral index of $\alpha \sim -1.4$ and an extrapolated 1.4 GHz flux density ~ 120 mJy. This value would be lowered to 40 mJy if a nominal synchrotron spectral index of $\alpha_{NT} = -0.8$ is assumed between 1.4 and 8 GHz. Using the scaling relations, these values correspond to kinetic jet power of $0.6\text{–}3 \times 10^{43}\ \mathrm{erg\ s}^{-1}$. As noted in Venturi et al. (2021), jet power may be underestimated by an order of magnitude using the above scaling relations compared to values derived from models of jet–ISM interaction (e.g., Mukherjee et al. 2018). The kinetic power of the outflow is several orders of magnitude smaller than the jet power, implying that the jet can perturb the gas in its vicinity, increasing its turbulence and thus being the main source of the low-velocity and high-dispersion outflow observed in the Paα emission line.

5. Summary

In this paper, we report JWST NIRSpec IFS observations of NGC 7469. With the superb spatial and spectral resolutions of NIRSpec, it is now possible to study in detail the inner kiloparsec of this galaxy. This allows us to unveil the intricate connection between the feeding, feedback, and gas excitation in the inner kiloparsec of this luminous Seyfert 1.5 galaxy. Our conclusions are summarized below.

1. Enhanced line ratios, consistent with shock-heated gas, are observed mostly in the nuclear region of the galaxy, with the highest line ratios to the west of the nucleus. The presence of a compact (<100 pc) radio jet (e.g., Lonsdale et al. 2003) indicates that its interaction with the gas in the inner-ISM region may be the cause of the H_2 and [Fe II] gas excitation. The spatially resolved excitation map also reveals diffuse AGN-like excitation over the FOV suggesting that the central source ionizes a significant fraction of the gas in the inner-ISM.

2. NGC 7469's kinematics are dominated by rotation (with amplitudes $\sim 150\ \mathrm{km\ s}^{-1}$ at a low-velocity dispersion of 60–80 km s^{-1}), especially in the star-forming ring region. We identify a nuclear spiral in NGC 7469 in the Paα velocity dispersion map. We interpret the nuclear spiral and the nonrotational motions (observed after modeling the rotation field) as a gas inflow to the nucleus of the galaxy. We estimate a mass inflow rate of 0.2–17 $M_\odot$ yr^{-1} dependent upon the precise geometry and inclination of the disk. This value is up to 2 orders of magnitude higher than the gas accretion rate needed to power the central AGN but comparable with the mass outflow rate.

3. The Paα emission line has a kinematical component consistent with an ionized gas outflow. This outflow is dominated by turbulent motions. It carries a kinetic power of $5.9\text{–}7.2 \times 10^{36}\ \mathrm{erg\ s}^{-1}$, which is consistent with being driven by a compact nuclear radio jet with a power of $10^{43}\ \mathrm{erg\ s}^{-1}$.

(NED), which is operated by the Jet Propulsion Laboratory, California Institute of Technology, under contract with the National Aeronautics and Space Administration.

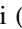*Facilities:* JWST (NIRSpec IFU and NIRCam), HST (WFC3), MAST, NED.

Software: Astropy (Astropy Collaboration et al. 2013, 2018, 2022), IFSCUBE (Ruschel-Dutra & Dall'Agnol De Oliveira 2020; Ruschel-Dutra et al. 2021), JWST Science Calibration (Bushouse et al. 2022), Matplotlib (Hunter 2007), QFitsView (Ott 2012), SciPy (Virtanen et al. 2020).

ORCID iDs

Marina Bianchin ⬧ https://orcid.org/0000-0002-6570-9446
Vivian U ⬧ https://orcid.org/0000-0002-1912-0024
Yiqing Song ⬧ https://orcid.org/0000-0002-3139-3041
Thomas S.-Y. Lai (賴劭愉) ⬧ https://orcid.org/0000-0001-8490-6632
Raymond P. Remigio ⬧ https://orcid.org/0000-0002-0164-8795
Loreto Barcos-Muñoz ⬧ https://orcid.org/0000-0003-0057-8892
Tanio Díaz-Santos ⬧ https://orcid.org/0000-0003-0699-6083
Lee Armus ⬧ https://orcid.org/0000-0003-3498-2973
Hanae Inami ⬧ https://orcid.org/0000-0003-4268-0393
Kirsten L. Larson ⬧ https://orcid.org/0000-0003-3917-6460
Aaron S. Evans ⬧ https://orcid.org/0000-0003-2638-1334
Torsten Böker ⬧ https://orcid.org/0000-0002-5666-7782
Justin A. Kader ⬧ https://orcid.org/0000-0002-6650-3757
Sean T. Linden ⬧ https://orcid.org/0000-0002-1000-6081
Vassilis Charmandaris ⬧ https://orcid.org/0000-0002-2688-1956
Matthew A. Malkan ⬧ https://orcid.org/0000-0001-6919-1237
Jeff Rich ⬧ https://orcid.org/0000-0002-5807-5078
Thomas Bohn ⬧ https://orcid.org/0000-0002-4375-254X
Anne M. Medling ⬧ https://orcid.org/0000-0001-7421-2944
Sabrina Stierwalt ⬧ https://orcid.org/0000-0002-2596-8531
Joseph M. Mazzarella ⬧ https://orcid.org/0000-0002-8204-8619
David R. Law ⬧ https://orcid.org/0000-0002-9402-186X
George C. Privon ⬧ https://orcid.org/0000-0003-3474-1125
Susanne Aalto ⬧ https://orcid.org/0000-0002-5828-7660
Philip Appleton ⬧ https://orcid.org/0000-0002-7607-8766
Victorine A. Buiten ⬧ https://orcid.org/0009-0003-4835-2435
Luke Finnerty ⬧ https://orcid.org/0000-0002-1392-0768
Christopher C. Hayward ⬧ https://orcid.org/0000-0003-4073-3236
Justin Howell ⬧ https://orcid.org/0000-0001-6028-8059
Kazushi Iwasawa ⬧ https://orcid.org/0000-0002-4923-3281
Francisca Kemper ⬧ https://orcid.org/0000-0003-2743-8240
Jed McKinney ⬧ https://orcid.org/0000-0002-6149-8178
Francisco Müller-Sánchez ⬧ https://orcid.org/0000-0002-2713-0628
Eric J. Murphy ⬧ https://orcid.org/0000-0001-7089-7325
Paul P. van der Werf ⬧ https://orcid.org/0000-0001-5434-5942
David B. Sanders ⬧ https://orcid.org/0000-0002-1233-9998
Jason Surace ⬧ https://orcid.org/0000-0001-7291-0087

References

Aalto, S., Muller, S., König, S., et al. 2019, A&A, 627, A147
Alberdi, A., Colina, L., Torrelles, J. M., et al. 2006, ApJ, 638, 938
Appleton, P. N., Guillard, P., Emonts, B., et al. 2023, ApJ, 951, 27
Armus, L., Lai, T. U. V., et al. 2023, ApJL, 942, L37
Arribas, S., Colina, L., Bellocchi, E., Maiolino, R., & Villar-Martín, M. 2014, A&A, 568, A14
Astropy Collaboration, Price-Whelan, A. M., Lim, P. L., et al. 2022, ApJ, 935, 167
Astropy Collaboration, Price-Whelan, A. M., Sipőcz, B. M., et al. 2018, AJ, 156, 123
Astropy Collaboration, Robitaille, T. P., Tollerud, E. J., et al. 2013, A&A, 558, A33
Barcos-Muñoz, L., Aalto, S., Thompson, T. A., et al. 2018, ApJL, 853, L28
Bertola, F., Bettoni, D., Danziger, J., et al. 1991, ApJ, 373, 369
Bianchin, M., Riffel, R. A., Storchi-Bergmann, T., et al. 2022, MNRAS, 510, 639
Bîrzan, L., McNamara, B. R., Nulsen, P. E. J., Carilli, C. L., & Wise, M. W. 2008, ApJ, 686, 859
Bohn, T., Inami, H., Diaz-Santos, T., et al. 2023, ApJL, 942, L36
Böker, T., Arribas, S., Lützgendorf, N., et al. 2022, A&A, 661, A82
Bouchet, P., García-Marín, M., Lagage, P. O., et al. 2015, PASP, 127, 612
Bushouse, H., Eisenhamer, J., Dencheva, N., et al. 2022, JWST Calibration Pipeline, v1.8.2, Zenodo, doi:10.5281/ZENODO.7325378
Cavagnolo, K. W., McNamara, B. R., Nulsen, P. E. J., et al. 2010, ApJ, 720, 1066
Clavijo-Bohórquez, W. E., de Gouveia Dal Pino, E. M., & Melioli, C. 2024, MNRAS
Colina, L., Piqueras López, J., Arribas, S., et al. 2015, A&A, 578, A48
Davies, R. I., Tacconi, L. J., & Genzel, R. 2004, ApJ, 602, 148
de Vaucouleurs, G., de Vaucouleurs, A., Corwin, H. G. J., et al. 1991, Third Reference Catalogue of Bright Galaxies (Berlin: Springer)
Díaz-Santos, T., Alonso-Herrero, A., Colina, L., Ryder, S. D., & Knapen, J. H. 2007, ApJ, 661, 149
Falstad, N., Aalto, S., Mangum, J. G., et al. 2018, A&A, 609, A75
Feruglio, C., Maiolino, R., Piconcelli, E., et al. 2010, A&A, 518, L155
Fiore, F., Feruglio, C., Shankar, F., et al. 2017, A&A, 601, A143
Forbes, D. A., & Ward, M. J. 1993, ApJ, 416, 150
García-Bernete, I., Rigopoulou, D., Alonso-Herrero, A., et al. 2022, A&A, 666, L5
González-Alfonso, E., Pereira-Santaella, M., Fischer, J., et al. 2021, A&A, 645, A49
Harrison, C. M., Alexander, D. M., Mullaney, J. R., & Swinbank, A. M. 2014, MNRAS, 441, 3306
Hekatelyne, C., Riffel, R. A., Sales, D., et al. 2018, MNRAS, 479, 3966
Hekatelyne, C., Riffel, R. A., Storchi-Bergmann, T., et al. 2020, MNRAS, 498, 2632
Hicks, E. K. S., & Malkan, M. A. 2008, ApJS, 174, 31
Hollenbach, D., & McKee, C. F. 1989, ApJ, 342, 306
Hunter, J. D. 2007, CSE, 9, 90
Hutchison, T. A., Welch, B. D., Rigby, J. R., et al. 2023, arXiv:2312.12518
Jakobsen, P., Ferruit, P., Alves de Oliveira, C., et al. 2022, A&A, 661, A80
Kakkad, D., Mainieri, V., Vietri, G., et al. 2020, A&A, 642, A147
Lai, T. S. Y., Armus, L., Bianchin, M., et al. 2023, ApJL, 957, L26
Lai, T. S. Y., Armus, L. U. V., U, V., et al. 2022, ApJL, 941, L36
Landt, H., Bentz, M. C., Ward, M. J., et al. 2008, ApJS, 174, 282
Larkin, J. E., Armus, L., Knop, R. A., Soifer, B. T., & Matthews, K. 1998, ApJS, 114, 59
Lonsdale, C. J., Lonsdale, C. J., Smith, H. E., & Diamond, P. J. 2003, ApJ, 592, 804
Lu, K.-X., Wang, J.-G., Zhang, Z.-X., et al. 2021, ApJ, 918, 50
Lutz, D., Sturm, E., Janssen, A., et al. 2020, A&A, 633, A134
Markwardt, C. B. 2009, in ASP Conf. Ser. 411, Astronomical Data Analysis Software and Systems XVIII, ed. D. A. Bohlender, D. Durand, & P. Dowler (San Francisco, CA: ASP), 251
Medling, A. M., Privon, G. C., Barcos-Muñoz, L., et al. 2019, ApJL, 885, L21
Medling, A. M. U. V., Rich, J. A., et al. 2015, MNRAS, 448, 2301
Morganti, R., Oosterloo, T., Oonk, J. B. R., Frieswijk, W., & Tadhunter, C. 2015, A&A, 580, A1
Morganti, R., Veilleux, S., Oosterloo, T., Teng, S. H., & Rupke, D. 2016, A&A, 593, A30
Motter, J. C., Riffel, R., Ricci, T. V., et al. 2021, MNRAS, 506, 4354
Mukherjee, D., Wagner, A. Y., Bicknell, G. V., et al. 2018, MNRAS, 476, 80
Müller-Sánchez, F., Prieto, M. A., Hicks, E. K. S., et al. 2011, ApJ, 739, 69
Orienti, M., & Prieto, M. A. 2010, MNRAS, 401, 2599
Osterbrock, D. E. 1977, ApJ, 215, 733
Osterbrock, D. E., & Ferland, G. J. 2006, Astrophysics of Gaseous Nebulae and Active Galactic Nuclei (Melville, NY: AIP)
Ott, T., 2012 QFitsView: FITS file viewer, Astrophysics Source Code Library, record, ascl:1210.019
Pereira-Santaella, M., Colina, L., García-Burillo, S., et al. 2020, A&A, 643, A89

Pérez-Torres, M., Mattila, S., Alonso-Herrero, A., Aalto, S., & Efstathiou, A. 2021, A&ARv, 29, 2

Peterson, B. M., Grier, C. J., Horne, K., et al. 2014, ApJ, 795, 149

Raimundo, S. I., Vestergaard, M., Koay, J. Y., et al. 2019, MNRAS, 486, 123

Reunanen, J., Kotilainen, J. K., & Prieto, M. A. 2002, MNRAS, 331, 154

Rich, J. A., Kewley, L. J., & Dopita, M. A. 2014, ApJL, 781, L12

Rich, J. A., Kewley, L. J., & Dopita, M. A. 2015, ApJS, 221, 28

Rich, J. A., Torrey, P., Kewley, L. J., Dopita, M. A., & Rupke, D. S. N. 2012, ApJ, 753, 5

Rieke, M. J., Kelly, D. M., Misselt, K., et al. 2023, PASP, 135, 028001

Riffel, R., Rodríguez-Ardila, A., Aleman, I., et al. 2013, MNRAS, 430, 2002

Riffel, R. A., Bianchin, M., Riffel, R., et al. 2021a, MNRAS, 503, 5161

Riffel, R. A., Riffel, R., Bianchin, M., et al. 2023a, MNRAS, 521, 3260

Riffel, R. A., Storchi-Bergmann, T., & Riffel, R. 2015, MNRAS, 451, 3587

Riffel, R. A., Storchi-Bergmann, T., Riffel, R., et al. 2021b, MNRAS, 504, 3265

Riffel, R. A., Storchi-Bergmann, T., Riffel, R., et al. 2023b, MNRAS, 521, 1832

Riffel, R. A., Storchi-Bergmann, T., Zakamska, N. L., & Riffel, R. 2020, MNRAS, 496, 4857

Rigby, J., Perrin, M., McElwain, M., et al. 2023, PASP, 135, 048001

Robleto-Orús, A. C., Torres-Papaqui, J. P., Longinotti, A. L., et al. 2021, ApJL, 906, L6

Rodríguez-Ardila, A., Pastoriza, M. G., Viegas, S., Sigut, T. A. A., & Pradhan, A. K. 2004, A&A, 425, 457

Rodríguez-Ardila, A., Prieto, M. A., Viegas, S., & Gruenwald, R. 2006, ApJ, 653, 1098

Rodríguez-Ardila, A., Riffel, R., & Pastoriza, M. G. 2005, MNRAS, 364, 1041

Rosenberg, M. J. F., van der Werf, P. P., & Israel, F. P. 2012, A&A, 540, A116

Rupke, D. S. N., & Veilleux, S. 2011, ApJL, 729, L27

Ruschel-Dutra, D., & Dall'Agnol De Oliveira, B. 2020, danielrd6/ifscube: Modeling, v1.1, Zenodo, doi:10.5281/zenodo.4065550

Ruschel-Dutra, D., Storchi-Bergmann, T., Schnorr-Müller, A., et al. 2021, MNRAS, 507, 74

Sanders, D. B., & Mirabel, I. F. 1996, ARA&A, 34, 749

Schnorr-Müller, A., Storchi-Bergmann, T., Ferrari, F., & Nagar, N. M. 2017, MNRAS, 466, 4370

Schnorr-Müller, A., Storchi-Bergmann, T., Robinson, A., Lena, D., & Nagar, N. M. 2016, MNRAS, 457, 972

Simpson, C., Forbes, D. A., Baker, A. C., & Ward, M. J. 1996, MNRAS, 283, 777

Song, Y., Linden, S. T., Evans, A. S., et al. 2021, ApJ, 916, 73

Song, Y., Linden, S. T., Evans, A. S., et al. 2022, ApJ, 940, 52

Storchi-Bergmann, T., Dors, O. L. J., Riffel, R. A., et al. 2007, ApJ, 670, 959

Storchi-Bergmann, T., McGregor, P. J., Riffel, R. A., et al. 2009, MNRAS, 394, 1148

Su, R., Mahony, E. K., Gu, M., et al. 2023, MNRAS, 520, 5712

U, V., Lai, T., Bianchin, M., et al. 2022, ApJL, 940, L5

U, V., Medling, A., Sanders, D., et al. 2013, ApJ, 775, 115

U, V., Medling, A. M., Inami, H., et al. 2019, ApJ, 871, 166

Veilleux, S., Bolatto, A., Tombesi, F., et al. 2017, ApJ, 843, 18

Venturi, G., Cresci, G., Marconi, A., et al. 2021, A&A, 648, A17

Virtanen, P., Gommers, R., Oliphant, T. E., et al. 2020, NatMe, 17, 261

Xu, C. K., Cao, C., Lu, N., et al. 2014, ApJ, 787, 48

Xu, X., & Wang, J. 2022, ApJ, 933, 110

Zhang, L., & Ho, L. C. 2023, ApJL, 953, L9